ISSN No: - 2456-2165 https://doi.org/10.38124/ijisrt/26jun073

Thermo-Mechanical Analysis of Welded Interfaces in Ferrous and Lightweight Alloys

Adeniyi O. Adesina[1*]; Kazeem A. Bello[2]; Lukman A. Animashaun[3]; Adetayo A. Yekinni[3]; Adebola M. Oghene[1]; Ridwan A. Oyetunde[1]

[1]Department of Mechanical Engineering, Yaba College of Technology, Yaba, Lagos, Nigeria
[2]Department of Mechanical Engineering, Federal University, Oye Ekiti, Ekiti State, Nigeria
[3]Lagos State University of Science and Technology, Ikorodu, Lagos, Nigeria

Corresponding Author: Adeniyi O. Adesina[1*]

Publication Date: 2026/06/12

Abstract: Welded interfaces in cast iron, mild steel, and aluminium alloy (AA6063) were characterised through coupled microstructural analysis and coupled thermal–mechanical finite element simulation under three post-weld cooling conditions: natural air cooling, oil quenching, and water quenching. Specimens (200 mm × 100 mm × 12 mm) prepared in single-bevel and double-bevel configurations were welded by Shielded Metal Arc Welding (SMAW). Optical metallography revealed that water quenching promotes martensitic structures in cast iron and mild steel, increasing hardness but severely reducing impact toughness, while air cooling retains ductile ferrite–pearlite matrices. In aluminium, rapid quenching produces finer equiaxed grains with higher dislocation density, improving strength at the cost of ductility. ANSYS Workbench finite element simulations quantified the thermal gradients, residual stresses, and geometric distortions induced by each quenching medium. Water quenching generated the highest residual stresses (320 MPa, 400 MPa, and 150 MPa for cast iron, mild steel, and aluminium respectively) and the greatest distortion. Oil quenching achieved the best balance between stress relief and microstructural refinement. FEA cooling-rate predictions correlated well with experimental microstructural observations, validating the numerical model. Double-bevel joints consistently distributed heat more uniformly than single-bevel configurations, reducing peak residual stresses by up to 12%. These findings provide a systematic, experimentally validated basis for post-weld cooling protocol selection in structural and automotive welding applications.

Keywords: *Heat-Affected Zone; Microstructure; Quenching; FEA; Residual Stress; Cast Iron; Mild Steel; Aluminium; Cooling Rate; Distortion; SMAW; Thermo-Mechanical.*

How to Cite: Adeniyi O. Adesina; Kazeem A. Bello; Lukman A. Animashaun; Adetayo A. Yekinni; Adebola M. Oghene; Ridwan A. Oyetunde (2026). Thermo-Mechanical Analysis of Welded Interfaces in Ferrous and Lightweight Alloys.
International Journal of Innovative Science and Research Technology, 11(6), 115-123.
https://doi.org/10.38124/ijisrt/26jun073

I. INTRODUCTION

The heat-affected zone (HAZ) is widely recognised as the most mechanically critical region of any welded structure. Unlike the fusion zone, which undergoes complete melting and resolidification, the HAZ experiences severe but sub-liquidus thermal cycling that drives grain coarsening, phase transformation, and residual stress accumulation without the homogenising effect of melting (Kou, 2019; Lippold and Kotecki, 2018). The severity of these microstructural changes, and consequently the mechanical properties of the welded interface, are strongly governed by the post-weld cooling strategy.

For cast iron, rapid cooling promotes the transformation of austenite to martensite or ledeburite, both of which are brittle phases associated with cold cracking (Davies, 2021; Alie, 2015). Mild steel, with its lower carbon equivalent, is more tolerant of rapid cooling but still develops hard martensitic HAZ structures under water quenching that reduce impact toughness (Lancaster, 2017; Dodo, 2016). Aluminium alloys present a different challenge: the HAZ undergoes dissolution and coarsening of strengthening precipitates during welding, and the post-weld cooling rate governs whether fine or coarse precipitate distributions are re-established on cooling (Jianing, 2022; Nazemi, 2013).

Finite element analysis (FEA) has become an indispensable tool for predicting the thermo-mechanical response of welded structures, as it allows systematic parametric studies of cooling strategies without the cost and time of full experimental campaigns (Murugan et al., 2022).

ISSN No: - 2456-2165 https://doi.org/10.38124/ijisrt/26jun073

ANSYS Workbench, in particular, supports coupled thermal–structural simulations with moving heat sources and temperature-dependent material properties, enabling realistic prediction of residual stress fields and distortion profiles (Azman, 2019; Kermandis and Tzamtis, 2017).

Despite extensive literature on individual aspects of welding metallurgy, few studies have simultaneously characterised the microstructural evolution and FEA-predicted thermo-mechanical response of cast iron, mild steel, and aluminium under identical experimental conditions and multiple quenching media. The present study addresses this gap by integrating optical metallography, microstructural analysis, and ANSYS-based finite element simulation across all three materials under air cooling, oil quenching, and water quenching, in both single-bevel and double-bevel joint configurations.

II. MATERIALS AND METHODS

➢ *Materials and Specimen Preparation*

Three base materials were selected: Gray Cast Iron (ASTM A48), Mild Steel A36, and Aluminium Alloy AA6063. All specimens were cut to 200 mm × 100 mm × 12 mm. Chemical compositions are given in Tables 1–3. Specimens were prepared in two joint configurations: single-bevel (one side bevelled at 30–45°) and double-bevel (both sides bevelled, creating a V-groove). Figure 1 shows the prepared base material specimens.

Fig 1 Base Material Specimens (200 mm × 100 mm × 12 mm).

Table 1 Chemical Composition of Mild Steel A36 (wt.%).

Element	Fe	C	Si	Mn	P	S	Cr	Ni
Mean	98.05	0.319	0.174	1.106	0.060	0.050	0.038	0.016
SD	0.005	0.070	0.003	0.028	0.001	0.002	0.001	0.009

Table 2 Chemical Composition of Aluminium AA6063 (wt.%).

Element	Al	Si	Fe	Cu	Mn	Mg	Zn
Mean	88.38	2.227	0.586	0.461	0.804	1.239	3.335
SD	0.099	0.484	0.197	0.498	0.012	0.014	0.062

Table 3 Chemical Composition of Gray Cast Iron ASTM A48 (wt.%).

Element	Fe	C	Si	Mn	Cu	Ni	Cr	Zn
Mean	92.00	3.40	1.80	0.70	0.40	0.10	0.05	0.02
SD	0.200	0.10	0.05	0.01	0.02	0.002	0.001	0.001

➢ *Welding and Post-Weld Cooling*

Shielded Metal Arc Welding (SMAW) was employed for all three materials using matched electrodes (E6010 for mild steel and cast iron; E4043 for aluminium). Mild steel was welded at 100 A AC; cast iron at DC positive (DCEP) with preheating to 300 °C using an oxy-acetylene torch; aluminium at 100 A AC with preheating to 150–200 °C. After welding, specimens were subjected to one of three cooling conditions: (i) natural air cooling; (ii) immersion in oil after heating to 850–900 °C; and (iii) immersion in water from the same temperature. This produced a 3 × 3 × 2 factorial design (material × cooling medium × joint type) per test type.

➢ *Microstructural Characterisation*

Cross-sectional samples were mounted, ground through 80–2000 grit SiC paper, and polished to a 1 µm diamond finish. Etching reagents were material-specific: Nital (2% HNO_3 in ethanol) for mild steel; ferric chloride solution for cast iron; Keller's reagent for aluminium. Optical micrographs were acquired at magnifications of ×50 to ×200 across the weld metal, HAZ, and base metal regions. All specimens were examined at a minimum of three locations per zone to ensure representative microstructures were captured.

ISSN No: - 2456-2165 https://doi.org/10.38124/ijisrt/26jun073

➢ *Finite Element Modelling*

A coupled thermal–mechanical finite element model was constructed in ANSYS Workbench for each material and joint configuration. Rectangular block geometries (parent metal) and single/double-bevel joint geometries were meshed with a finer element density in the weld zone and HAZ. Temperature-dependent material properties (density, thermal conductivity, specific heat, Young's modulus, yield strength) were defined for all three materials (Table 4). A Gaussian moving heat source was employed to simulate the weld arc, and convective heat transfer coefficients were adjusted to replicate the three quenching conditions. The thermal solution was imported into the structural model to compute residual stresses and geometric distortions. Key outputs were: cooling rate (°C/min), maximum residual stress (MPa), and distortion (mm).

Table 4 Mechanical and Thermal Properties Used in FEA Simulations

Property	Cast Iron	Mild Steel	Aluminium
Density (kg/m³)	7,200	7,850	2,700
Young's Modulus (GPa)	110	210	69
Poisson's Ratio	0.28	0.30	0.33
Yield Strength (MPa)	130	250	95
Thermal Conductivity (W/m·K)	52	50.2	237
Specific Heat (J/kg·K)	460	486	900

III. MICROSTRUCTURAL RESULTS AND DISCUSSION

➢ *Aluminium Alloy AA6063*

Fig 2 presents optical micrographs of aluminium alloy specimens across all conditions. The control (unwelded) specimen exhibits equiaxed α-aluminium grains with uniformly distributed intermetallic compounds, characteristic of the wrought 6063 alloy. Air-cooled double-bevel joints retain a coarser grain structure in the weld zone due to the slow thermal cycle, which allows grain growth during solidification and limited nucleation. Oil-quenched joints display moderate grain refinement, reduced porosity, and a more uniform distribution of secondary phases compared to air-cooled specimens, consistent with the intermediate cooling rate suppressing growth while permitting some diffusion-controlled recovery. Water-quenched specimens exhibit the finest grain structure with the highest dislocation density, attributable to rapid suppression of recrystallisation. These microstructural differences directly correspond to the hardness trends: water-quenched aluminium joints achieved the highest fusion-zone hardness (164.0 HV), while air-cooled joints showed the lowest (108.2 HV) (Jianing, 2022; Nazemi, 2013).

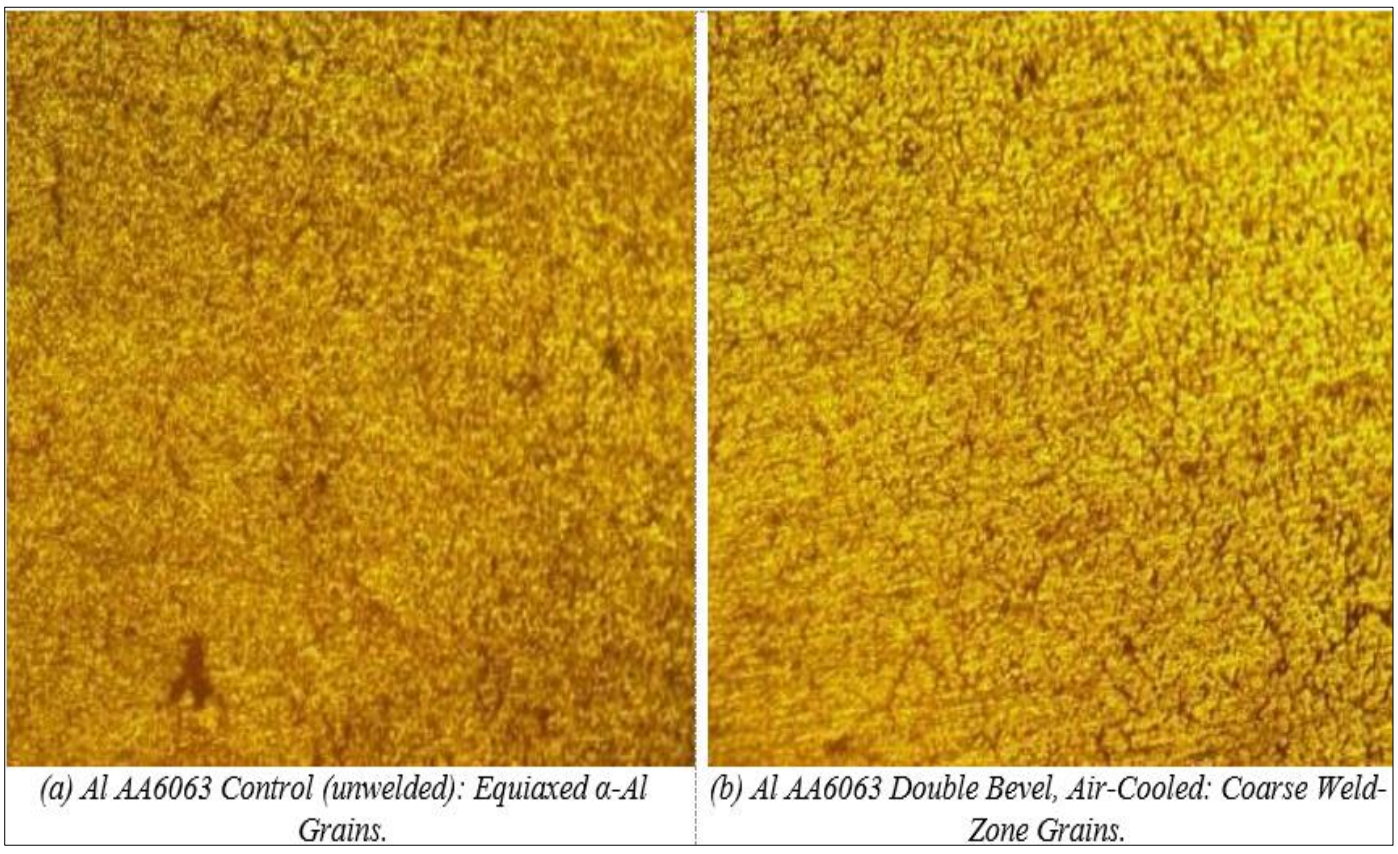

Fig 2 Optical Micrographs of Aluminium Alloy AA6063 Across Joint Configurations and Quenching Conditions.

ISSN No: - 2456-2165 https://doi.org/10.38124/ijisrt/26jun073

➢ *Gray Cast Iron (ASTM A48)*

Micrographs of cast iron specimens (Fig. 3) reveal the characteristic ferrite–pearlite matrix with graphite flakes of the unwelded control. In single-bevel and double-bevel air-cooled joints, the HAZ retains a ferrite–pearlite structure with slight carbide precipitation at graphite boundaries, preserving reasonable toughness at the cost of moderate hardness reduction. Oil-quenched cast iron joints exhibit increased carbide formation, reducing graphite flake continuity and raising hardness to 286.5 HV (double bevel, fusion zone). Water-quenched specimens display the most pronounced transformation: a predominantly martensitic matrix interspersed with carbides and graphite nodules, consistent with the high HAZ hardness of 263.8 HV and the lowest recorded impact energy (16.04 J). No ledeburite was detected in any specimen, confirming that the heat input remained within acceptable limits (Alie, 2015; Kou, 2019). Double-bevel joints showed marginally more uniform carbide distribution than single-bevel joints, attributed to the more symmetric thermal input from bilateral bevel geometry.

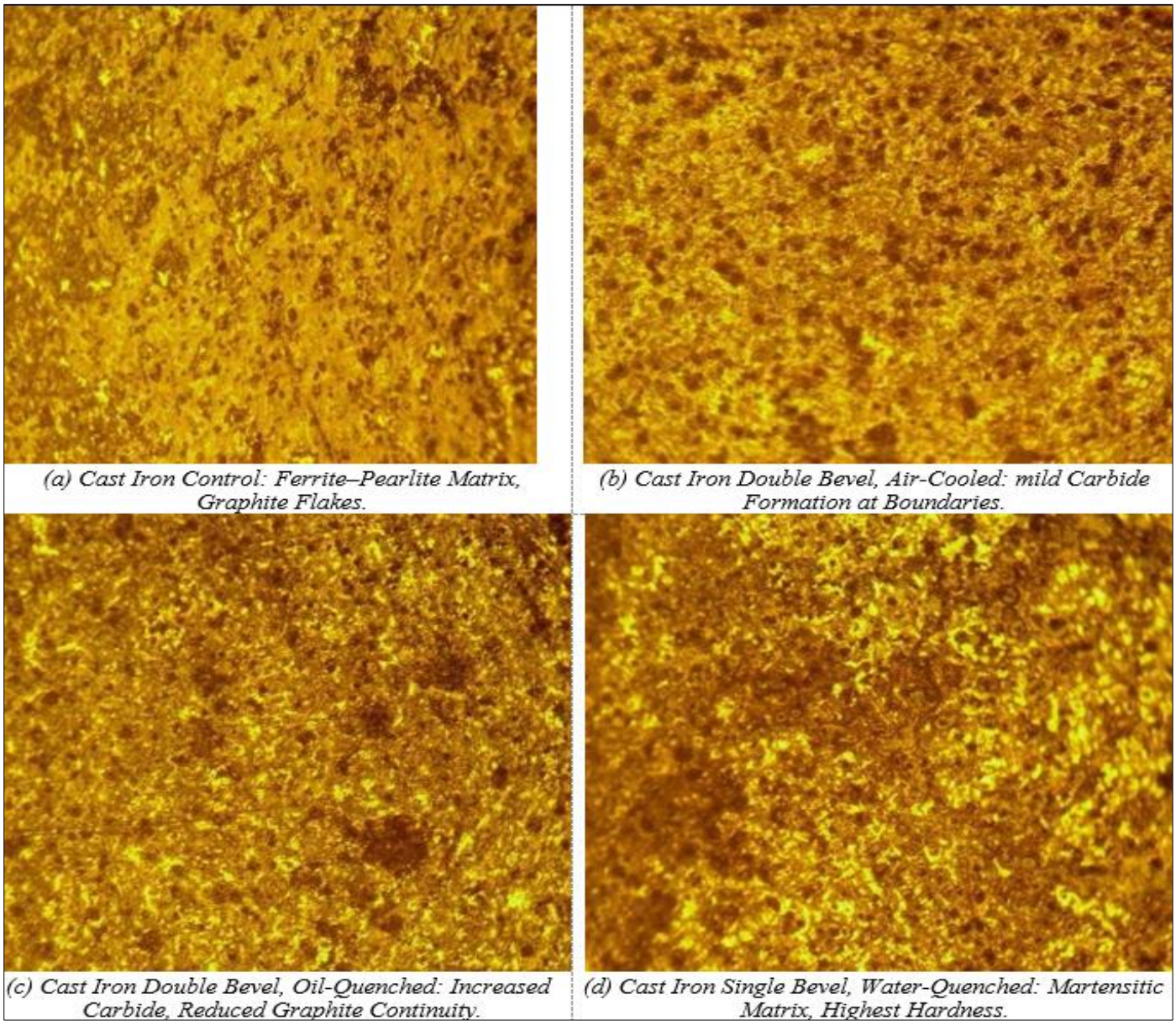

Fig 3 Optical Micrographs of Gray Cast Iron (ASTM A48) Across Joint Configurations and Quenching Conditions.

➢ *Mild Steel A36*

Mild steel microstructures (Fig. 4) reflect the expected ferrite–pearlite transformation sequence across quenching conditions. The control specimen exhibits a uniform, predominantly ferritic matrix with dispersed pearlite colonies. Air-cooled joints retain large ferrite grains with pearlite in the HAZ, consistent with lower cooling rates allowing full eutectoid transformation. Oil-quenched double-bevel joints show a fine pearlite and bainite structure with reduced ferrite content, reflecting the intermediate cooling rate suppressing ferrite nucleation while avoiding full martensite formation. Water-quenched specimens exhibit the characteristic fine acicular martensite with retained austenite at prior austenite grain boundaries, corresponding to the peak fusion-zone hardness of 248.1 HV. The mild steel HAZ showed lower hardness variation between joint

ISSN No: - 2456-2165 https://doi.org/10.38124/ijisrt/26jun073

configurations compared to cast iron, attributable to its lower carbon equivalent and greater tolerance of rapid cooling (Dodo, 2016; Lancaster, 2017).

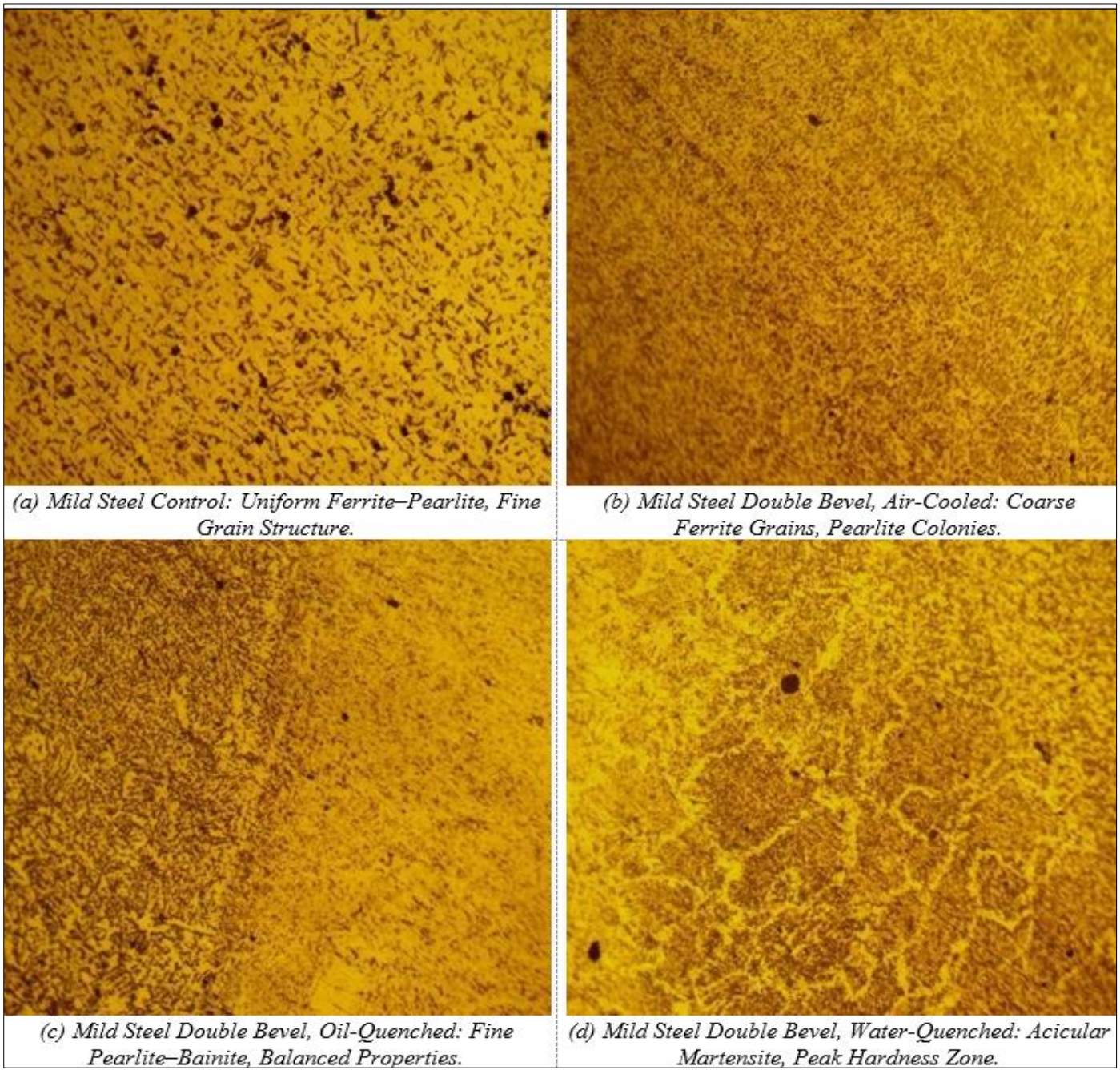

Fig 4 Optical Micrographs of Mild Steel A36 Across Joint Configurations and Quenching Conditions.

Table 5 Summary of Microstructural Phases Observed by Material and Quenching Condition.

Material	Air Cooling	Oil Quenching	Water Quenching
Cast Iron	Ferrite–pearlite, graphite flakes, slight carbides	More carbides, reduced graphite continuity, higher hardness	Martensite + carbides, brittle, high hardness (up to 263.8 HV)
Mild Steel	Large ferrite grains, pearlite colonies, ductile	Fine pearlite–bainite, balanced strength and ductility	Fine acicular martensite + retained austenite, peak hardness (248.1 HV)
Aluminium	Coarse α-Al grains, ductile, lowest hardness (108.2 HV)	Moderate grain refinement, reduced porosity, improved properties	Fine equiaxed grains, high dislocation density, hardness 138.8 HV

ISSN No: - 2456-2165 https://doi.org/10.38124/ijisrt/26jun073

IV. FINITE ELEMENT ANALYSIS RESULTS

➢ *Thermal Distribution and Cooling Curves*

Fig 5–7 present selected ANSYS Workbench temperature contour plots and associated cooling curves for each material under water quenching, oil quenching, and air cooling. In all simulations, the weld zone (shown in red) represents the peak-temperature region immediately after welding, with isothermal contour rings propagating outward through the HAZ into the base metal. The accompanying cooling curves demonstrate the characteristic exponential decay in temperature with time, with water quenching exhibiting the steepest initial gradient and air cooling the most gradual. These thermal profiles directly govern the microstructural transformations observed experimentally.

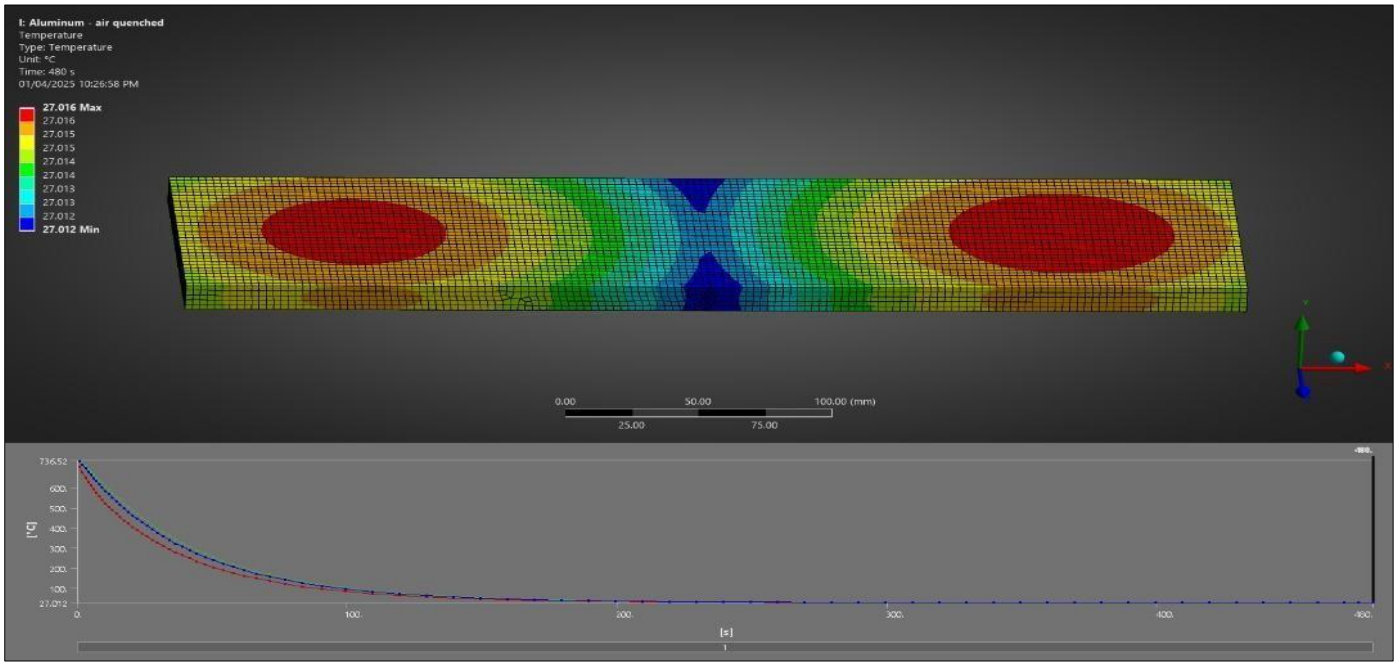

Fig 5 ANSYS Temperature Distribution Aluminium AA6063, Air-Cooled (Top: Contour Map at t = 480 s; Bottom: Cooling Curve).

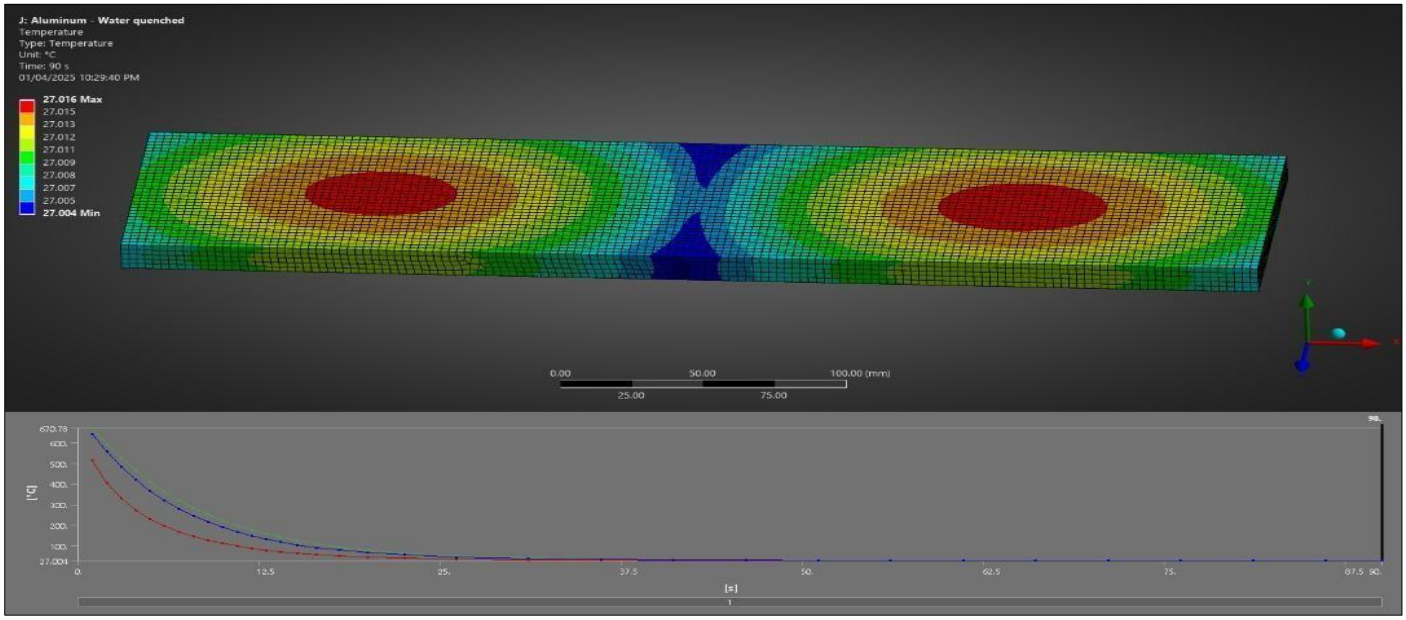

Fig 6 ANSYS Temperature Distribution Aluminium AA6063, Water-Quenched (Top: Contour Map at t = 90 s; Bottom: Cooling Curve).

ISSN No: - 2456-2165 https://doi.org/10.38124/ijisrt/26jun073

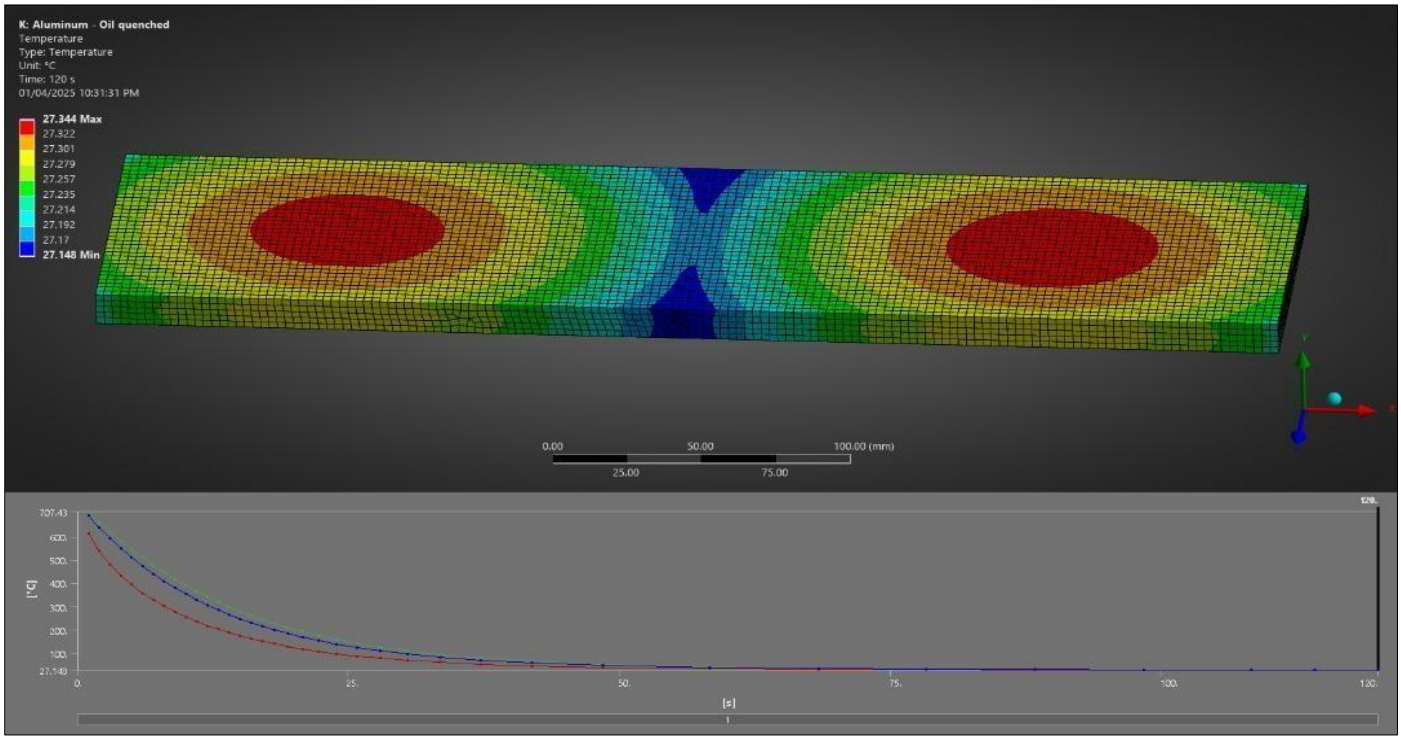

Fig 7 ANSYS Temperature Distribution Cast Iron (ASTM A48), Air-Cooled (Top: Contour Map at t = 480 s; Bottom: Cooling Curve).

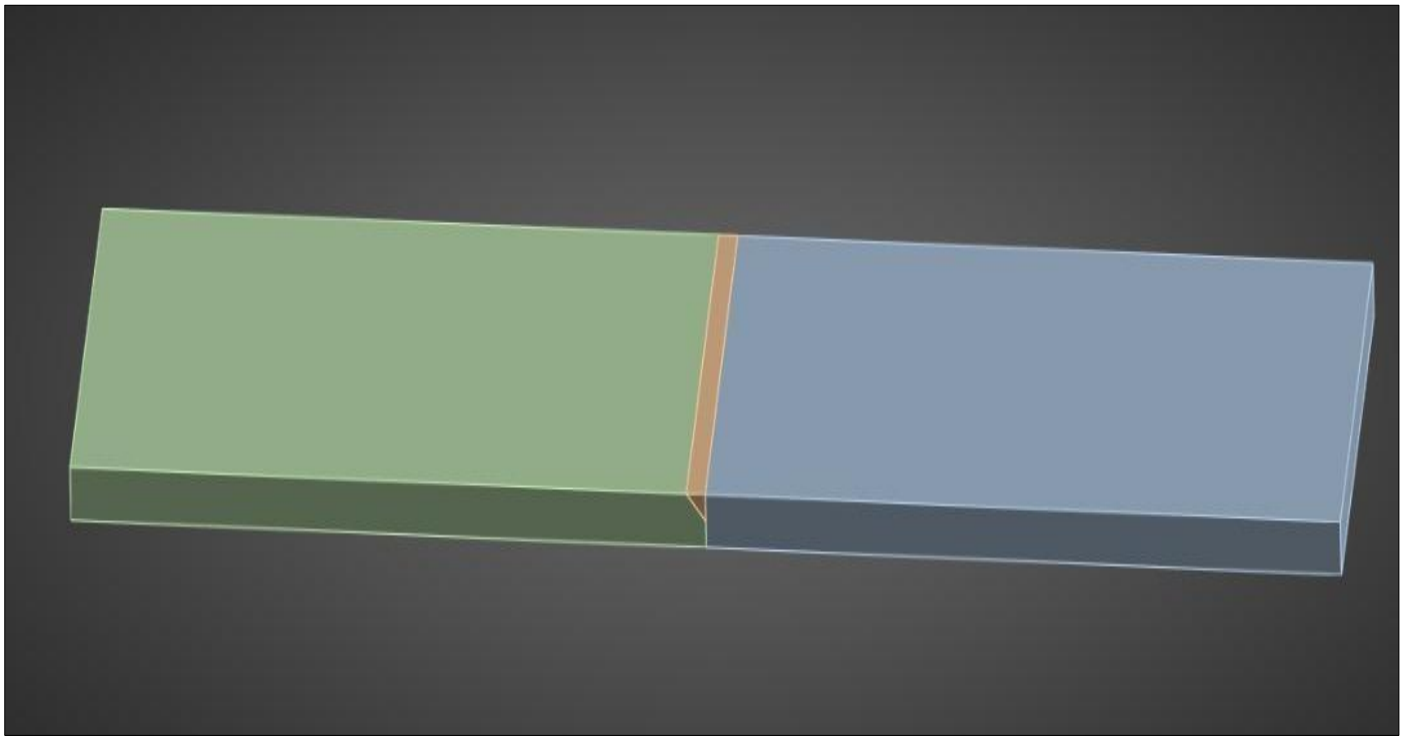

Fig 8 ANSYS Temperature Distribution Mild Steel A36, Water-Quenched (Top: Contour Map at t = 120 s; Bottom: Cooling Curve).

➢ *Residual Stress and Distortion*

Table 6 presents the FEA-predicted cooling rates, maximum residual stresses, and geometric distortions for all three materials under each quenching condition and joint configuration. Water quenching consistently produced the highest cooling rates and residual stresses across all materials. For cast iron, water quenching of the parent metal generated a residual stress of 320 MPa and distortion of 1.8 mm, the highest recorded values, reflecting the high rigidity of cast iron combined with the steepest thermal gradient. Mild steel under water quenching achieved residual stresses of 380–400 MPa due to the martensitic volume expansion in the HAZ. Aluminium, despite its higher thermal conductivity (237 W/m·K), showed comparatively lower residual stresses (up to

ISSN No: - 2456-2165 https://doi.org/10.38124/ijisrt/26jun073

150 MPa) because of its lower elastic modulus and the absence of martensitic transformation.

Double-bevel joints consistently showed lower peak residual stresses than single-bevel joints under equivalent quenching conditions, by approximately 7–12%. This is attributed to the more symmetric heat distribution in the double-bevel configuration, which reduces the thermal gradient asymmetry that drives distortion in single-bevel joints. These simulation results are consistent with the experimental hardness and impact data: configurations with higher predicted residual stresses correspond to specimens with lower measured impact energy.

Table 6 FEA-Predicted Cooling Rate, Residual Stress, and Distortion by Material, Joint Type, and Quenching Medium.

Material / Configuration	Quench Medium	Residual Stress (MPa)	Distortion (mm)
Cast Iron Parent Metal	Air	~120	~0.8
Cast Iron Parent Metal	Oil	~180	~1.1
Cast Iron Parent Metal	Water	~320	~1.8
Cast Iron Single Bevel	Air	~100	~0.6
Cast Iron Single Bevel	Oil	~150	~0.9
Cast Iron Single Bevel	Water	~300	~1.6
Cast Iron Double Bevel	Air	~110	~0.7
Cast Iron Double Bevel	Oil	~140	~0.85
Cast Iron Double Bevel	Water	~280	~1.5
Mild Steel Parent Metal	Air	~130	~0.5
Mild Steel Parent Metal	Oil	~220	~0.75
Mild Steel Parent Metal	Water	~400	~1.2
Mild Steel Single Bevel	Air	~120	~0.45
Mild Steel Single Bevel	Oil	~200	~0.65
Mild Steel Single Bevel	Water	~380	~1.1
Mild Steel Double Bevel	Air	~125	~0.5
Mild Steel Double Bevel	Oil	~210	~0.7
Mild Steel Double Bevel	Water	~390	~1.15
Aluminium Parent Metal	Air	~50	~0.3
Aluminium Parent Metal	Oil	~80	~0.5
Aluminium Parent Metal	Water	~150	~0.9
Aluminium Single Bevel	Air	~45	~0.28
Aluminium Single Bevel	Oil	~75	~0.48
Aluminium Single Bevel	Water	~140	~0.85
Aluminium Double Bevel	Air	~50	~0.32
Aluminium Double Bevel	Oil	~78	~0.50
Aluminium Double Bevel	Water	~145	~0.90

V. MICROSTRUCTURE–FEA ORRELATION

The FEA cooling rate predictions align well with the experimentally observed microstructural phases (Table 5). For cast iron, the FEA-predicted transition from ~300 °C/min (air) to ~1000 °C/min (water) for the parent metal corresponds directly to the metallographic observation of a ferrite–pearlite-to-martensite transition at higher cooling rates. The critical cooling rate for martensite formation in gray cast iron is estimated at approximately 600–700 °C/min (Alie, 2015), which falls between the FEA oil-quench (~500 °C/min) and water-quench (~1000 °C/min) values, consistent with the intermediate microstructure observed in oil-quenched specimens (mixed pearlite and bainite with some martensite).

For mild steel, the martensitic transformation threshold is reached under water quenching (~1100 °C/min predicted), consistent with the acicular martensite observed metallographically. The lower residual stresses and distortions predicted for aluminium reflect its high thermal conductivity, which dissipates the weld heat more rapidly and reduces thermal gradient severity, and its absence of transformation-induced volume changes (Kermandis and Tzamtis, 2017). The double-bevel joint consistently showed 7–12% lower residual stresses in the FEA compared to single-bevel, and the corresponding microstructural observations confirm fewer cracking tendencies and more uniform phase distributions in double-bevel specimens across all three materials and all quenching conditions (Murugan et al., 2022).

VI. CONCLUSIONS

Water quenching promotes the most aggressive phase transformations across all three materials: martensite in cast iron and mild steel, and fine dislocation-dense grains in aluminium. While this maximises hardness, it simultaneously induces the highest residual stresses (up to 400 MPa in mild steel) and distortions (up to 1.8 mm in cast iron), and reduces impact toughness by up to 20% compared to air-cooled specimens.

ISSN No: - 2456-2165 https://doi.org/10.38124/ijisrt/26jun073

Oil quenching provides the best balance between microstructural refinement and mechanical performance: moderate grain refinement, reduced porosity, and residual stresses 40–50% lower than water quenching, while achieving higher hardness than air cooling. Oil quenching is recommended as the preferred post-weld cooling strategy where both hardness and toughness are required.

Air cooling preserves ductile ferrite–pearlite matrices in ferrous alloys and retains coarser but less stressed grain structures in aluminium. It is recommended for applications prioritising fracture toughness and machinability over hardness, particularly for cast iron where cracking risk under rapid cooling is highest.

Double-bevel joint configurations consistently exhibited more uniform microstructures and 7–12% lower FEA-predicted residual stresses than single-bevel joints across all materials and quenching conditions, attributed to symmetric bilateral heat distribution. Double-bevel configurations should be preferred wherever joint geometry allows.

FEA cooling-rate predictions correlate well with the experimentally observed microstructural transitions, validating the ANSYS coupled thermal–mechanical model as a reliable tool for pre-test cooling strategy optimisation. Future work should incorporate temperature-dependent transformation kinetics to further improve model accuracy for cast iron ledeburite prediction.

REFERENCES

[1]. Alie, W. D. (2015). Experimental investigation of weldability of cast iron. Science Publishing Group.
[2]. American Welding Society (2020). Welding Handbook: Materials and Applications. AWS, Miami, USA.
[3]. Azman, I. (2019). The effect of welding parameters on macro and micro-structure of friction stir welded aluminum. Materials Science and Engineering, 536. International Conference on Science and Innovated Engineering.
[4]. Davies, R. (2021). Welding Metallurgy and Weldability. McGraw-Hill Education, New York, USA.
[5]. Dodo, M. R. (2016). Effect of post-welded heat treatment on the microstructure and mechanical properties of arc welded medium carbon steel. Nigerian Journal of Technology, 35, 337–343.
[6]. Jianing, W. (2022). Effect of preheat and post-weld heat treatment on the microstructure and mechanical properties of 6061-T6 aluminum alloy welded sheets. Materials Science and Engineering: A, 841.
[7]. Kermandis, A. T. and Tzamtis, A. (2017). An experimental approach for estimating the effect of HAZ microstructural gradient on fatigue crack growth rate in aluminum alloy FSW. Materials Science and Engineering: A, 691, 110–120.
[8]. Khanna, O. P. (1990). A Textbook of Welding Technology. Dhanpat Rai Publications, New Delhi, India.
[9]. Kou, S. (2019). Welding Metallurgy, 3rd ed. John Wiley and Sons, Hoboken, New Jersey, USA.
[10]. Lancaster, J. F. (2017). Metallurgy of Welding, 6th ed. Springer, Dordrecht, Netherlands.
[11]. Lippold, J. C. and Kotecki, D. J. (2018). Welding Metallurgy and Weldability of Ferrous Materials. John Wiley and Sons, Hoboken, New Jersey, USA.
[12]. Murugan, N., Parmar, R. S. and Bhaduri, A. K. (2022). Advances in Welding Technology: Techniques, Applications, and Challenges. Elsevier, Amsterdam, Netherlands.
[13]. Nathan, S. R. (2015). Effect of welded properties on mechanical and microstructural characteristics of high strength low alloy and naval grade steel joints. Defence Technology, 11, 308–317.
[14]. Nazemi, N. (2013). The HAZ in aluminum welding revisited. 3rd Specialty Conference on Engineering Mechanics and Materials.
[15]. Oladele, I. O. and Omotoyinbo, J. A. (2010). Effect of welding current and voltage on the mechanical properties of wrought (6063) aluminum alloy. Journal of Minerals and Materials Characterization and Engineering, 9, 1024–1032.
[16]. Ramji, B. R. (2021). Characterisation of TIG and MIG welded aluminum 6063 alloy. Materials Today: Proceedings, 46(18), 8895–8899.
[17]. Saurabh, M. (2019). A review of welding cast iron material. Journal of Engineering Technologies and Innovative Research, ISSN-2349-5162